REPORT

SOLAR CELLS

Efficient and stable solution-processed planar perovskite solar cells via contact passivation

Hairen Tan,[1] Ankit Jain,[1] Oleksandr Voznyy,[1] Xinzheng Lan,[1] F. Pelayo García de Arquer,[1] James Z. Fan,[1] Rafael Quintero-Bermudez,[1] Mingjian Yuan,[1] Bo Zhang,[1] Yicheng Zhao,[1] Fengjia Fan,[1] Peicheng Li,[2] Li Na Quan,[1] Yongbiao Zhao,[2] Zheng-Hong Lu,[2] Zhenyu Yang,[1] Sjoerd Hoogland,[1] Edward H. Sargent[1]*

Planar perovskite solar cells (PSCs) made entirely via solution processing at low temperatures (<150°C) offer promise for simple manufacturing, compatibility with flexible substrates, and perovskite-based tandem devices. However, these PSCs require an electron-selective layer that performs well with similar processing. We report a contact-passivation strategy using chlorine-capped TiO_2 colloidal nanocrystal film that mitigates interfacial recombination and improves interface binding in low-temperature planar solar cells. We fabricated solar cells with certified efficiencies of 20.1 and 19.5% for active areas of 0.049 and 1.1 square centimeters, respectively, achieved via low-temperature solution processing. Solar cells with efficiency greater than 20% retained 90% (97% after dark recovery) of their initial performance after 500 hours of continuous room-temperature operation at their maximum power point under 1-sun illumination (where 1 sun is defined as the standard illumination at AM1.5, or 1 kilowatt/square meter).

Metal halide perovskite solar cells (PSCs) have attracted extensive research interest for next-generation solution-processed photovoltaic (PV) devices because of their high solar-to-electric power conversion efficiency (PCE) and low fabrication cost (*1*–*4*). The top-performing PSCs, which have reached a certified PCE of 22.1%, have relied on high-temperature–sintered (450° to 550°C) mesoporous TiO_2 as the electron-selective layer (ESL) (*5*–*7*). However, this high-temperature processing makes manufacture more complex and hampers the development of flexible modules and perovskite-based monolithic tandem devices. To overcome this limitation, researchers have pursued planar PSCs that exploit low-temperature (typically <150°C) solution-processed charge-selective layers. Metal oxide materials such as TiO_2, ZnO, SnO_2, and Zn_2SnO_4 colloidal nanoparticles synthesized at low temperatures have commonly been used as the ESL (*8*–*16*). Very recently, high-efficiency (certified 19.9%), small-area PSCs have been achieved using low-temperature–processed SnO_2 (*17*, *18*).

Unfortunately, long-term device operational stability has remained far inferior to that of counterpart devices made using high-temperature–processed ESLs (*19*–*22*). Furthermore, the high efficiency and large area required for industrialization have yet to be demonstrated in low-temperature planar PSCs (table S5) (*23*–*25*).

We reasoned that performance and stability loss in low-temperature planar PSCs could arise from imperfect interfaces and charge recombination between the selective contact at the illumination side and the perovskite film grown on top (*4*, *26*, *27*), as the perovskite active layers themselves have excellent long-term photostability upon the addition of formamidinium (FA), Cs, and Br ions (*19*–*22*, *28*). Once the impressively long photocarrier diffusion lengths in perovskite films are achieved, attention must shift to perfecting the interface (*29*–*32*). We reasoned that deep trap states present at the perovskite/ESL interface could potentially be addressed by passivating the interface between the charge-selective contact and the perovskite absorber.

We devised a simple and effective interface-passivation method that leads to efficient and stable low-temperature–processed planar PSCs. Chlorine-capped TiO_2 colloidal nanocrystal (NC) films processed at <150°C were used as the ESL. The chloride additive in perovskite precursor solutions enhances grain-boundary passivation in $MAPbI_{3-x}Cl_x$ (MA, methylammonium cation, $CH_3NH_3^+$) PSCs (*33*–*36*). We found that the interfacial Cl atoms on the TiO_2 NCs suppress deep trap states at the perovskite interface and thus considerably reduce interface recombination at the TiO_2/perovskite contact. The interfacial Cl atoms also lead to strong electronic coupling and chemical binding at the TiO_2/perovskite planar junction, as projected in previous theoretical studies (*37*). As a result, we fabricated hysteresis-free planar PSCs with independently certified PCEs of 20.1% for small-area devices (0.049 cm^2) and 19.5% for large-area devices (1.1 cm^2). The low-temperature planar PSCs with high initial PCE >20% exhibit excellent operational stability and retain 90% (97% after dark recovery) of their initial performance after 500 hours operating at their maximum power point (MPP) under constant 1-sun illumination (where 1 sun is defined as the standard illumination at AM1.5, or 1 kW/m^2).

We first used density functional theory (DFT) to examine defect passivation and interface binding by interfacial chlorine at the TiO_2/perovskite interface (Fig. 1, fig. S1, and table S1) (*38*). We found that Cl at the interface results in stronger binding at the TiO_2/perovskite interface for both the cases of MAX- and PbX_2-terminated (X = Cl, I) perovskite surfaces. Perovskite films with the PbX_2-terminated interface are energetically favored to contact the TiO_2. Previous studies (*39*–*41*) have shown that, in bulk perovskites, the most detrimental defects (deep-level defects) are antisites but that their formation energy is relatively high, which explains the low trap-state density in $MAPbI_3$ perovskite films and single crystals. Vacancies and interstitials, although much more abundant, are shallow defects. We thus explored the effect of Cl at the interface on both antisite and vacancy defects. Without Cl, a Pb-I antisite defect leads to localized states near the valence band edge (Fig. 1A). These states can capture holes and become nonradiative recombination centers. In contrast, the formation energy of the Pb-Cl antisite at the $PbCl_2$-terminated interface is higher (i.e., less favorable to form), which indicates that antisite defects are suppressed in the presence of interfacial Cl atoms. The Pb-Cl antisite defect becomes much shallower and more delocalized (Fig. 1B) and has little effect on interface recombination. Overall, the incorporation of Cl atoms at the TiO_2/perovskite interface resulted in a lower density of interfacial trap states (fig. S1, B and D), as well as stronger binding between TiO_2 and perovskite (table S1).

We devised a synthetic approach to obtain Cl-capped TiO_2 NCs as the ESL in solar cells. We first synthesized ~5-nm-diameter anatase TiO_2 NCs (fig. S2) (*38*) via a nonhydrolytic method through the reaction of $TiCl_4$ and benzyl alcohol at 85°C under ambient atmosphere (*42*, *43*). This process resulted in Cl-capped TiO_2 NCs (TiO_2-Cl) with 12 ± 2 atomic % of Cl relative to Ti atoms, as determined by x-ray photoelectron spectroscopy (XPS) (Fig. 1C). A mixture of methanol and chloroform was used to disperse the NCs while preserving surface Cl ligands. XPS confirmed that surface Cl ligands were well retained after we formed films from a methanol-chloroform cosolvent (Fig. 1C). In contrast, the surface Cl ligands were detached from TiO_2 surfaces when the washed NCs were redispersed in ethanol with a stabilizer such as titanium

[1]Department of Electrical and Computer Engineering, University of Toronto, 35 St. George Street, Toronto, Ontario M5S 1A4, Canada. [2]Department of Materials Science and Engineering, University of Toronto, 184 College Street, Toronto, Ontario M5S 3E4, Canada.
***Corresponding author. Email: ted.sargent@utoronto.ca**

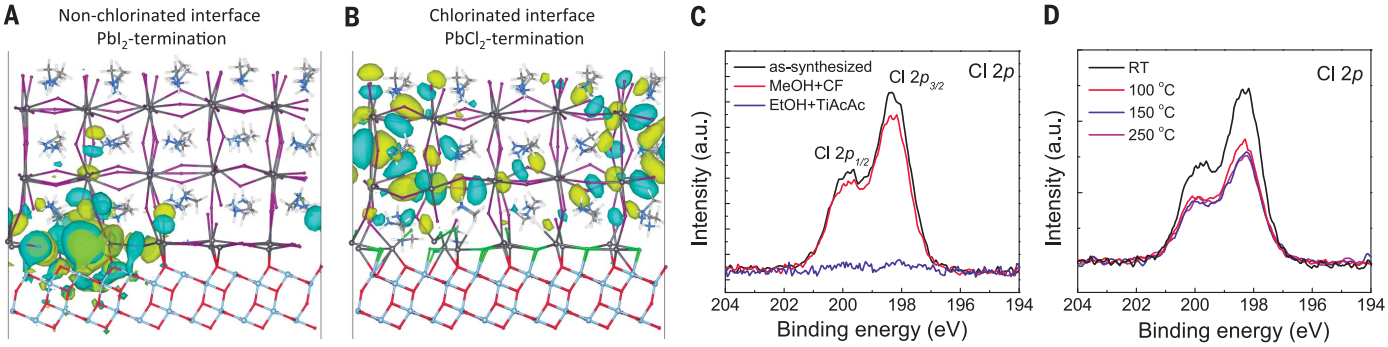

Fig. 1. The effect of Cl on interface quality between perovskite and TiO_2, and stabilization of Cl-capped TiO_2 (TiO_2-Cl) colloidal nanocrystals. (**A**) Trap-like localized antisite defects form near the valence band edge for the PbI_2-terminated TiO_2/perovskite interface. (**B**) Shallow and delocalized Pb-Cl antisite defects are seen for the $PbCl_2$-terminated interface. (**C** and **D**) XPS spectra of Cl 2p peaks of (C) TiO_2 NC films [as-synthesized, redispersed in the cosolvent of methanol and chloroform (MeOH + CF), and redispersed in ethanol with titanium diisopropoxide bis(acetylacetonate) as stabilizer (EtOH + TiAcAc)] and (D) TiO_2-Cl NC films with various post-annealing temperatures [room temperature (RT) and 100°, 150°, and 250°C]. a.u., arbitrary units.

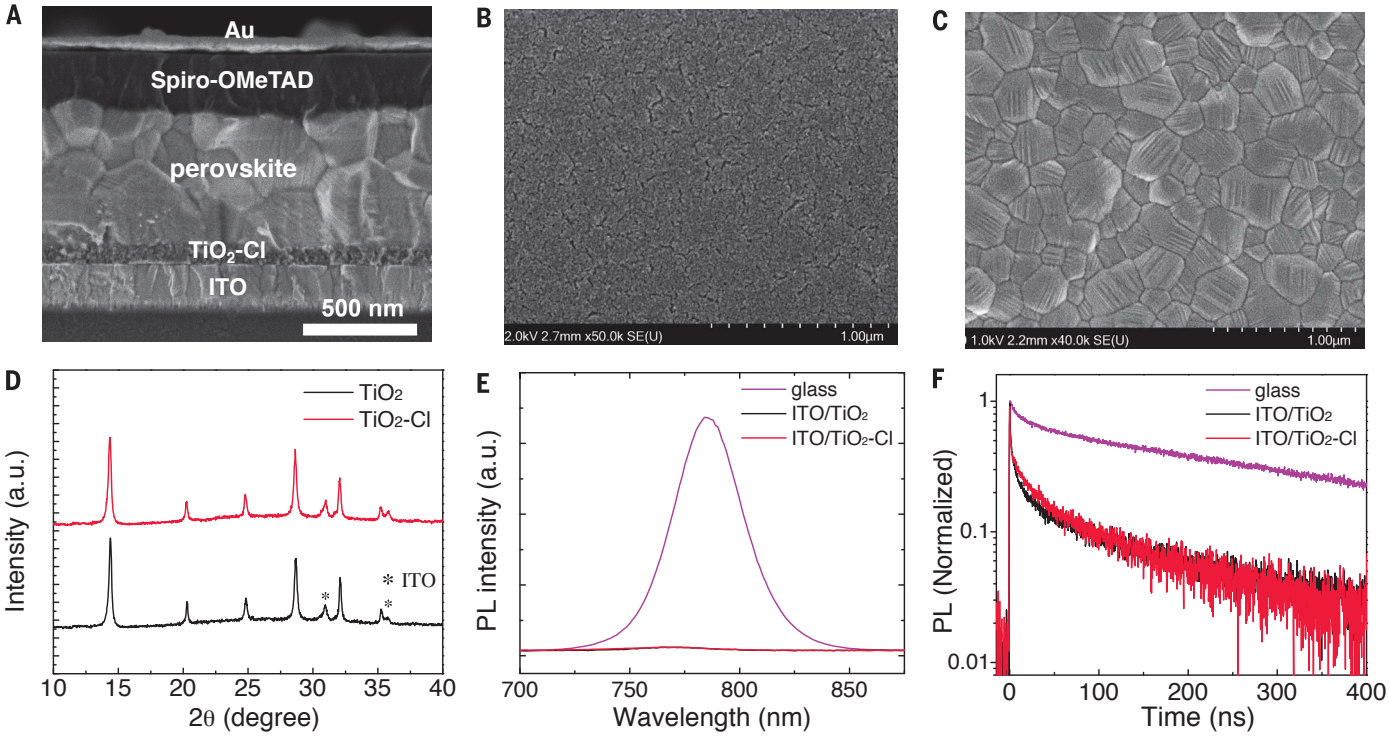

Fig. 2. Device structure and characterization of perovskite films on TiO_2-Cl. (**A**) Device structure and cross-sectional scanning electron microscopy (SEM) image of planar perovskite solar cells (PSCs). (**B** and **C**) Top-view SEM images of the TiO_2-Cl film on an ITO substrate (B) and the perovskite film on TiO_2-Cl (C). (**D**) XRD patterns of perovskite films on TiO_2 and TiO_2-Cl. (**E**) Steady-state PL spectra and (**F**) time-resolved PL decays of perovskite films on bare glass and on TiO_2- and TiO_2-Cl–coated ITO substrates. The PL signals of perovskite films on TiO_2 and TiO_2-Cl were effectively quenched by the fast charge extraction by TiO_2 and TiO_2-Cl.

diisopropoxide bis(acetylacetonate) (TiAcAc). Such TiO_2 NCs that lack Cl ligands—the ESL materials used in previous reports (*8*, *9*)—were taken as controls in the present study. Henceforth, we refer to the TiO_2 ESL with Cl ligands as TiO_2-Cl and the TiO_2 ESL lacking the Cl ligands as TiO_2. The Cl atoms were strongly bound to TiO_2, and the Cl ligands of TiO_2 thin film were retained on the surface after annealing up to 250°C (Fig. 1D).

We fabricated planar PSCs with TiO_2 as the ESL with the device architecture of Fig. 2A. The TiO_2-Cl film on indium tin oxide (ITO)–coated glass obtained by spin-coating was smooth and pinhole-free (Fig. 2B and fig. S3A). The film also exhibited negligible parasitic absorption loss over the entire visible–to–near-infrared spectral range (fig. S3B). Post-annealing treatment at moderate temperatures was applied to improve the quality of the spin-cast TiO_2-Cl film. The best PV performance was achieved with a TiO_2-Cl annealing temperature of 150°C (table S2 and fig. S4). The mixed cation-halide perovskite layer $FA_{0.85}MA_{0.15}PbI_{2.55}Br_{0.45}$, with a thickness of ~600 nm, was deposited on the TiO_2-Cl film using the antisolvent method (*38*, *44*, *45*). The processing solvent for perovskite precursors (e.g., dimethylsulfoxide) did not remove surface Cl ligands from the TiO_2-Cl film (fig. S5).

The bulk quality of perovskite films was similar on both TiO_2-Cl and TiO_2, a consequence of their identical processing. Smooth pinhole-free perovskite films with uniform and large grains were formed on both TiO_2-Cl and TiO_2 (Fig. 2C

and fig. S6). As expected from the stoichiometric ratio of the precursors, x-ray diffraction (XRD) spectra show no obvious PbI_2 nor other nonperovskite phases in films (Fig. 2D). The sharp absorption edge and narrow photoluminescence (PL) spectrum of the perovskite film confirm a homogenous and single-phase material (fig. S7). The perovskite films on both TiO_2-Cl and TiO_2 exhibit a very low trap-state density of ~3×10^{15} cm^{-3}, as determined using the space-charge limited current method (fig. S8). The band alignment between TiO_2-Cl (or TiO_2) and perovskite was determined from ultraviolet (UV) photoelectron spectroscopy and absorption measurements (fig. S9). The excellent match in conduction band minimum between TiO_2-Cl and perovskite allowed efficient electron transfer into TiO_2-Cl, whereas the high offset in valence band maximum provided efficient hole blocking.

We used steady-state and time-resolved PL spectroscopy to study the charge transfer kinetics between perovskite and ESLs. When perovskite films were formed on TiO_2 and TiO_2-Cl, the steady-state PL was quenched because of fast electron transfer to the ESLs (Fig. 2E). Figure 2F shows the PL decays of the perovskite films on bare glass and on the TiO_2- and TiO_2-Cl–coated ITO glass substrates. Table S3 summarizes the decays fit for biexponential components, a fast decay lifetime τ_1, and a slow decay lifetime τ_2. The perovskite film on bare glass had a long lifetime (τ_2) of 470 ns. The PL lifetimes of perovskite films on ESLs were shortened to a similar degree for both TiO_2 and TiO_2-Cl. This result indicates that both ESLs had sufficient electron extraction in solar cells, consistent with the good band alignments between the ESLs and perovskite.

To explore the effect of interfacial Cl atoms on the PV performance of planar PSCs, we made devices on the TiO_2-Cl and control TiO_2 ESLs. Figure S10 presents the statistical performance of 40 devices fabricated with otherwise-identical device processing on each type of ESL. Solar cells fabricated on TiO_2-Cl exhibit considerably better performance than those on TiO_2 for all PV metrics: The average open-circuit voltage (V_{oc}) increased from 1.06 to 1.14 V with the incorporation of Cl, and the average fill factor (*FF*) increased from 69 to 77%. Correspondingly, TiO_2-Cl resulted in a higher average PCE (19.8%) than the Cl-free TiO_2 (15.8%).

Device performance measured after optimization is shown in Fig. 3A and table S4. Our results confirm that the interfacial Cl atoms, not the bulk properties of TiO_2 ESLs, dominate the performance of these PSCs. Figure 3B shows a histogram of PCE values over 200 planar PSCs fabricated on TiO_2-Cl within a period of 3 months. Excellent reproducibility is indicated by the narrow distribution of PCE values. The best-performing devices with TiO_2-Cl reached a PCE of 20.9%. The PCE from current density–voltage (*J-V*) sweeps is consistent with the stabilized maximum power output (fig. S11). The external quantum efficiency (EQE) spectrum (fig. S12) exhibited a broad plateau above 80% over the spectral range from 400 to 760 nm because of strong light harvesting within the thick perovskite film. Integration of the EQE curve with the AM1.5G solar spectrum yielded a photocurrent density of 22.6 mA cm^{-2}, in good agreement with the short-circuit current density (J_{sc}) value from *J-V* characterization. We also examined the hysteresis of solar cells made on TiO_2-Cl and TiO_2 (Fig. 3A and table S4). Devices on TiO_2-Cl showed negligible hysteresis, whereas devices made on TiO_2 exhibit strong hysteresis, similar to previous studies using low-temperature TiO_2 as the ESL (*8*, *9*). The PV parameters of the Cl-free devices varied substantially with respect to scan direction.

To gain further insight into the performance enhancement resulting from the use of TiO_2-Cl, we characterized perovskite film properties, charge-transfer kinetics, and charge recombination in solar cells with TiO_2 and TiO_2-Cl. The bulk quality of perovskite films and charge transfer

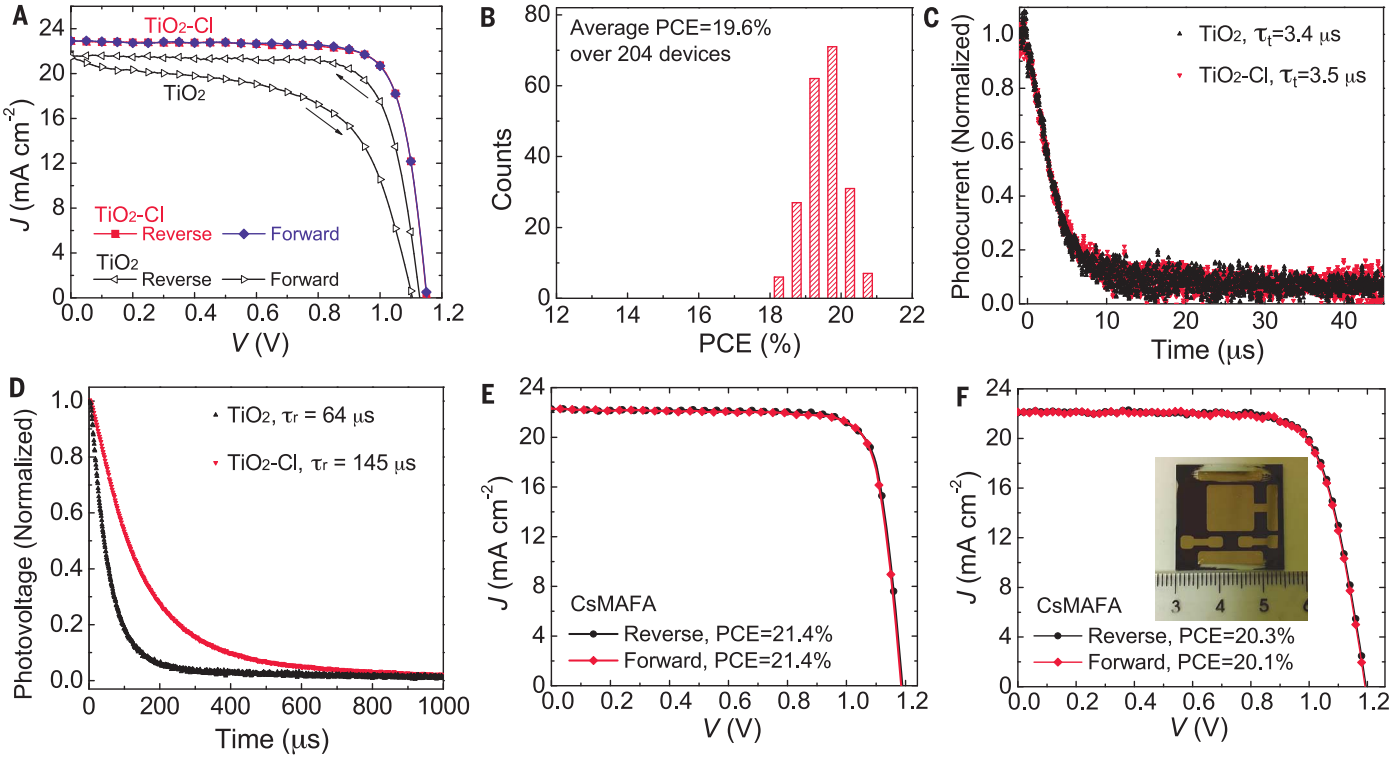

Fig. 3. Enhanced photovoltaic performance of perovskite solar cells with TiO_2-Cl. (**A**) *J-V* curves of PSCs with TiO_2 and TiO_2-Cl as electron-selective layers (ESLs) measured at reverse and forward scans. (**B**) Histogram of the power conversion efficiency (PCE) values among 204 devices on TiO_2-Cl. (**C**) Normalized transient photocurrent decay and (**D**) normalized transient photovoltage decay of solar cells with TiO_2 and TiO_2-Cl as ESLs. Devices shown in (A) to (D) have the perovskite composition of MAFA. τ_t, charge-transport lifetime; τ_r, charge-recombination lifetime. (**E**) *J-V* curves of the best-performing small-area (0.049 cm^2) CsMAFA PSC measured at reverse and forward scans. (**F**) *J-V* curves of the best-performing large-area (1.1 cm^2) CsMAFA PSC, showing a PCE of 20.3% (V_{oc} = 1.196 V, J_{sc} = 22.2 mA cm^{-2}, *FF* = 76.4%) at the reverse scan. The inset shows a photo of the large-area device. MAFA and CsMAFA denote the perovskite compositions of $FA_{0.85}MA_{0.15}PbI_{2.55}Br_{0.45}$ and $Cs_{0.05}FA_{0.81}MA_{0.14}PbI_{2.55}Br_{0.45}$, respectively.

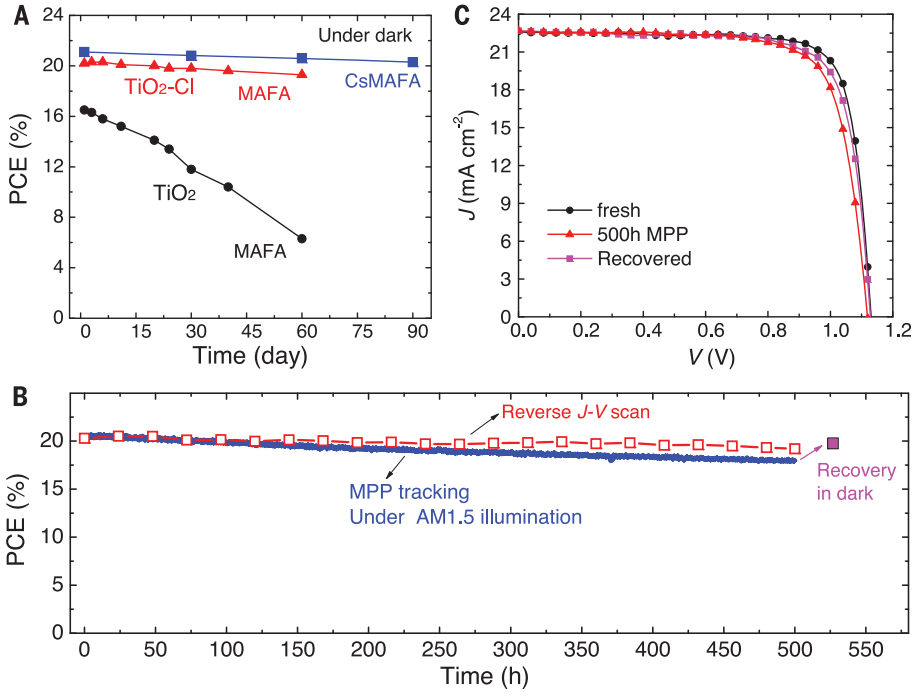

Fig. 4. Long-term device stability of perovskite solar cells with TiO_2-Cl and TiO_2. (**A**) Dark storage stability of nonencapsulated PSCs using TiO_2 and TiO_2-Cl. The unsealed cells were kept in a dry cabinet (<30% relative humidity) in the dark and measured regularly in nitrogen. PCE values were obtained from the reverse scans. (**B**) Continuous maximum power point (MPP) tracking for 500 hours of a high-performance unsealed CsMAFA cell with TiO_2-Cl in nitrogen atmosphere under constant simulated solar illumination (100 mW cm^{-2}) with a 420-nm cutoff UV filter. PCE values taken from reverse *J-V* scans (square symbols) are shown as well; the device retains 95% of its initial performance, as determined from reverse *J-V* scans. (**C**) *J-V* curves of the PSC (CsMAFA) from (B) at various stages:

were similar on both ESLs. Transient photocurrent decay under short-circuit conditions was obtained to study the influence of the ESL on charge transfer in solar cells (Fig. 3C). Cells with the two ESLs had a comparable charge-transport lifetime (τ_t ~ 3.4 μs), indicating similar interfacial charge transfer. This similarity implies that either bulk quality or interfacial charge transfer is not the main reason for the solar cell performance enhancement by TiO_2-Cl.

We used transient photovoltage decay under the open-circuit condition to characterize solar cells and found that the charge-recombination lifetime (τ_r) of the device on TiO_2-Cl was substantially longer than that of the device on TiO_2 (145 versus 64 μs) (Fig. 3D), consistent with slowed charge recombination at the TiO_2-Cl/perovskite interface. The reduced ideality factor of solar cells with TiO_2-Cl (n = 1.25) compared to those with TiO_2 (n = 1.73) is consistent with suppressed interfacial recombination (fig. S13). As seen in the DFT studies, interfacial Cl atoms suppress the formation of deep trap states on the surface of perovskite films, leading to improved surface passivation and reduced interfacial recombination.

To examine the applicability of TiO_2-Cl to other high-efficiency PSCs, we fabricated devices using cesium-containing perovskite $Cs_{0.05}FA_{0.81}MA_{0.14}PbI_{2.55}Br_{0.45}$ (denoted as CsMAFA), which had been shown to improve performance and photostability compared with $FA_{0.85}MA_{0.15}PbI_{2.55}Br_{0.45}$ (denoted as MAFA) (*22*, *46*, *47*). The best-performing small-area CsMAFA solar cell (0.049 cm^2) exhibited a high laboratory PCE of 21.4% (V_{oc} = 1.189 V, J_{sc} = 22.3 mA/cm^2, FF = 0.806) without hysteresis in *J-V* sweeps (Fig. 3E). We also fabricated large-area (1.1 cm^2) CsMAFA solar cells on TiO_2-Cl, showing a PCE value >20% with negligible hysteresis (Fig. 3F). A small-area and a large-area device were sent, without encapsulation, to an accredited independent PV test laboratory (Newport Corporation PV Lab, Montana, USA) for certification. These devices produced certified PCEs of 20.1 and 19.5%, respectively (figs. S14 to S16). The large-area device exhibited ~3% performance loss relative to the small-area device. The certified PCE of 19.5% for the large-area, low-temperature planar PSC exceeds that of other reported low-temperature or planar PSCs (*24*, *25*), and it approaches the certified PCE of large-area cells that relied on high-temperature–sintered mesoporous TiO_2 (table S5) (*23*, *38*, *48*).

We examined the long-term stability of low-temperature planar PSCs made on TiO_2-Cl and TiO_2 under dark storage as well as under operating conditions. The long-term stability of PSCs is closely related to the front ESL/perovskite interface binding strength and interfacial charge accumulation during operation (*49*, *50*). The devices made on TiO_2-Cl showed substantially enhanced stability relative to TiO_2 under dark storage (Fig. 4A). MAFA-based devices on TiO_2-Cl maintained 95% of their initial PCE after storage in the dark over 60 days, whereas those on TiO_2 only retained 38% of their initial efficiency (Fig. 4A). The high-efficiency CsMAFA devices on TiO_2-Cl (initial PCE > 21%) exhibited promising shelf stability, retaining 96% of their initial performance after 90 days (more than 2000 hours).

Solar cells must operate stably under MPP conditions. The MAFA solar cells based on TiO_2-Cl showed improved stability under continuous operation at MPP, as compared with devices based on TiO_2 (fig. S17). The CsMAFA solar cells on TiO_2-Cl (with a 420-nm cutoff UV filter) retained 90% of their initial performance after continuous operation for 500 hours under 1-sun illumination, as directly determined from the MPP tracking (Fig. 4B). The PCE increased slightly in the first tens of hours of MPP operation, which may be caused by light-induced defect healing in the perovskite active layer (*19*, *51*). No perovskite decomposition was observed after MPP operation, as seen from the XRD results (fig. S18), which indicates that the performance drop during MPP operation may be caused by defect generation in the perovskite layer (*52*, *53*) and changes to the perovskite/spiro-OMeTAD interface (the latter has previously been shown to be vulnerable) (*54*–*56*). The device self-recovered to an efficiency of 19.8% (97% of initial PCE) following dark storage (Fig. 4C), consistent with previous reports (*18*, *19*, *52*).

Overall, the stronger binding at the TiO_2-Cl/perovskite interface and the suppressed interfacial recombination account for superior stability in planar PSCs based on TiO_2-Cl. The new approach to fabricate efficient and stable PSCs is simple and scalable, compatible with future industrialization of perovskite-based PV technology. It offers a promising path to flexible devices and, in combination with low–band-gap semiconductor materials, to the formation of tandem devices.

REFERENCES AND NOTES

1. S. D. Stranks, H. J. Snaith, *Nat. Nanotechnol.* **10**, 391–402 (2015).
2. M. A. Green, A. Ho-Baillie, H. J. Snaith, *Nat. Photonics* **8**, 506–514 (2014).
3. Y. Zhao, K. Zhu, *Chem. Soc. Rev.* **45**, 655–689 (2016).
4. N. Park, M. Grätzel, T. Miyasaka, K. Zhu, K. Emery, *Nat. Energy* **1**, 16152 (2016).
5. W. S. Yang *et al.*, *Science* **348**, 1234–1237 (2015).
6. D. Bi *et al.*, *Nat. Energy* **1**, 16142 (2016).
7. D.-Y. Son *et al.*, *Nat. Energy* **1**, 16081 (2016).
8. H. Zhou *et al.*, *Science* **345**, 542–546 (2014).
9. K. Wojciechowski, M. Saliba, T. Leijtens, A. Abate, H. J. Snaith, *Energy Environ. Sci.* **7**, 1142–1147 (2014).
10. S. S. Shin *et al.*, *Nat. Commun.* **6**, 7410 (2015).
11. D. Liu, T. L. Kelly, *Nat. Photonics* **8**, 133–138 (2013).
12. J. You *et al.*, *Nat. Nanotechnol.* **11**, 75–81 (2016).
13. X. Liu *et al.*, *Adv. Mater. Interfaces* **3**, 1600122 (2016).
14. Z. Zhu *et al.*, *Adv. Mater.* **28**, 6478–6484 (2016).
15. T. A. Berhe *et al.*, *Energy Environ. Sci.* **9**, 323–356 (2016).

16. H. Kim, K.-G. Lim, T.-W. Lee, *Energy Environ. Sci.* **9**, 12–30 (2016).
17. Q. Jiang *et al.*, *Nat. Energy* **2**, 16177 (2016).
18. E. H. Anaraki *et al.*, *Energy Environ. Sci.* **9**, 3128–3134 (2016).
19. M. Saliba *et al.*, *Science* **354**, 206–209 (2016).
20. W. Chen *et al.*, *Science* **350**, 944–948 (2015).
21. A. Mei *et al.*, *Science* **345**, 295–298 (2014).
22. M. Saliba *et al.*, *Energy Environ. Sci.* **9**, 1989–1997 (2016).
23. X. Li *et al.*, *Science* **353**, 58–62 (2016).
24. Y. Wu *et al.*, *Nat. Energy* **1**, 16148 (2016).
25. J. Werner *et al.*, *ACS Energy Lett.* **1**, 474–480 (2016).
26. T. Singh, J. Singh, T. Miyasaka, *ChemSusChem* **9**, 2559–2566 (2016).
27. N. Ahn *et al.*, *Nat. Commun.* **7**, 13422 (2016).
28. H. Tsai *et al.*, *Nature* **536**, 312–316 (2016).
29. Y. Shao, Y. Yuan, J. Huang, *Nat. Energy* **1**, 15001 (2016).
30. Q. Wang, Q. Dong, T. Li, A. Gruverman, J. Huang, *Adv. Mater.* **28**, 6734–6739 (2016).
31. Y. Li *et al.*, *J. Am. Chem. Soc.* **137**, 15540–15547 (2015).
32. F. Giordano *et al.*, *Nat. Commun.* **7**, 10379 (2016).
33. D. W. de Quilettes *et al.*, *Science* **348**, 683–686 (2015).
34. Q. Chen *et al.*, *Nat. Commun.* **6**, 7269 (2015).
35. D. E. Starr *et al.*, *Energy Environ. Sci.* **8**, 1609–1615 (2015).
36. J. Chae, Q. Dong, J. Huang, A. Centrone, *Nano Lett.* **15**, 8114–8121 (2015).
37. E. Mosconi, E. Ronca, F. De Angelis, *J. Phys. Chem. Lett.* **5**, 2619–2625 (2014).
38. See supplementary materials.
39. W. Yin, T. Shi, Y. Yan, *Appl. Phys. Lett.* **104**, 063903 (2014).
40. A. Buin *et al.*, *Nano Lett.* **14**, 6281–6286 (2014).
41. W. Yin, J. Yang, J. Kang, Y. Yan, S.-H. Wei, *J. Mater. Chem. A Mater. Energy Sustain.* **3**, 8926–8942 (2015).
42. M. Niederberger, M. H. Bartl, G. D. Stucky, *Chem. Mater.* **14**, 4364–4370 (2002).
43. J. Wang, J. Polleux, J. Lim, B. Dunn, *J. Phys. Chem. C* **111**, 14925–14931 (2007).
44. N. J. Jeon *et al.*, *Nat. Mater.* **13**, 897–903 (2014).
45. D. Bi *et al.*, *Sci. Adv.* **2**, e1501170 (2016).
46. J.-W. Lee *et al.*, *Adv. Energy Mater.* **5**, 1501310 (2015).
47. Z. Li *et al.*, *Chem. Mater.* **28**, 284–292 (2016).
48. M. A. Green, K. Emery, Y. Hishikawa, W. Warta, E. D. Dunlop, *Prog. Photovolt. Res. Appl.* **24**, 905–913 (2016).
49. W. Tress, J. P. Correa Baena, M. Saliba, A. Abate, M. Graetzel, *Adv. Energy Mater.* **6**, 1600396 (2016).
50. Y. Yuan, J. Huang, *Acc. Chem. Res.* **49**, 286–293 (2016).
51. E. Mosconi, D. Meggiolaro, H. J. Snaith, S. D. Stranks, F. De Angelis, *Energy Environ. Sci.* **9**, 3180–3187 (2016).
52. W. Nie *et al.*, *Nat. Commun.* **7**, 11574 (2016).
53. D. W. deQuilettes *et al.*, *Nat. Commun.* **7**, 11683 (2016).
54. K. Domanski *et al.*, *ACS Nano* **10**, 6306–6314 (2016).
55. A. Guerrero *et al.*, *ACS Nano* **10**, 218–224 (2016).
56. Z. Hawash, L. K. Ono, S. R. Raga, M. V. Lee, Y. Qi, *Chem. Mater.* **27**, 562–569 (2015).

ACKNOWLEDGMENTS

This publication is based, in part, on work supported by an award (KUS-11-009-21) from the King Abdullah University of Science and Technology, by the Ontario Research Fund Research Excellence Program, by the Ontario Research Fund, and by the Natural Sciences and Engineering Research Council of Canada. H.T. acknowledges the Netherlands Organisation for Scientific Research (NWO) for a Rubicon grant (680-50-1511) to support his postdoctoral research at the University of Toronto. The work of A.J. is supported by the IBM Canada Research and Development Center through the Southern Ontario Smart Computing Innovation Platform (SOSCIP) postdoctoral fellowship. F.P.G.A. acknowledges funding from the Connaught program. DFT calculations were performed on the IBM BlueGene Q supercomputer with support from the SOSCIP. We thank R. Wolowiec, E. Palmiano, D. Kopilovic, and J. Li for their help during the course of study. All data are reported in the main text and supplementary materials.

SUPPLEMENTARY MATERIALS

www.sciencemag.org/content/355/6326/722/suppl/DC1
Materials and Methods
Figs. S1 to S18
Tables S1 to S5
References (*57*–*59*)

29 August 2016; resubmitted 6 December 2016
Accepted 23 January 2017
Published online 2 February 2017
10.1126/science.aai9081

Science

Efficient and stable solution-processed planar perovskite solar cells via contact passivation

Hairen Tan, Ankit Jain, Oleksandr Voznyy, Xinzheng Lan, F. Pelayo García de Arquer, James Z. Fan, Rafael Quintero-Bermudez, Mingjian Yuan, Bo Zhang, Yicheng Zhao, Fengjia Fan, Peicheng Li, Li Na Quan, Yongbiao Zhao, Zheng-Hong Lu, Zhenyu Yang, Sjoerd Hoogland and Edward H. Sargent

Science **355** (6326), 722-726.
DOI: 10.1126/science.aai9081originally published online February 2, 2017

Passivating traps in perovskites

Low-temperature processing of planar organic-inorganic perovskite solar cells made through solution processing would allow for simpler manufacturing and the use of flexible substrates. However, materials currently in use form interfaces with charge carrier trap states that limit performance. Tan *et al.* used chlorine-capped TiO_2 colloidal nanocrystal films as an electron-selective layer, which limited interface recombination in solution-processed solar cells. Such cells achieved certified efficiencies of 19.5% for active areas of 1.1 cm^2.

Science, this issue p. 722